Wiley Online Library
Early View publication on www.wileyonlinelibrary.com
(issue and page numbers not yet assigned;
citable using Digital Object Identifier – **DOI**)

Laser Photonics Rev., 1–13 (2015) / **DOI** 10.1002/lpor.201500031

LASER & PHOTONICS REVIEWS

Abstract Near-field optical microscopy techniques provide information on the amplitude and phase of local fields in samples of interest in nanooptics. However, the information on the near field is typically obtained by converting it into propagating far fields where the signal is detected. This is the case, for instance, in polarization-resolved scattering-type scanning near-field optical microscopy (s-SNOM), where a sharp dielectric tip scatters the local near field off the antenna to the far field. Up to now, basic models have interpreted *S*- and *P*-polarized maps obtained in s-SNOM as directly proportional to the in-plane (E_x or E_y) and out-of-plane (E_z) near-field components of the antenna, respectively, at the position of the probing tip. Here, a novel model that includes the multiple-scattering process of the probing tip and the nanoantenna is developed, with use of the reciprocity theorem of electromagnetism. This novel theoretical framework provides new insights into the interpretation of s-SNOM near-field maps: the model reveals that the fields detected by polarization-resolved interferometric s-SNOM do not correlate with a single component of the local near field, but rather with a complex combination of the different local near-field components at each point (E_x, E_y and E_z). Furthermore, depending on the detection scheme (*S*- or *P*-polarization), a different scaling of the scattered fields as a function of the local near-field enhancement is obtained. The theoretical findings are corroborated by s-SNOM experiments which map the near field of linear and gap plasmonic antennas. This new interpretation of nanoantenna s-SNOM maps as a complex-valued combination of vectorial local near fields is crucial to correctly understand scattering-type near-field microscopy measurements as well as to interpret the signals obtained in field-enhanced spectroscopy.

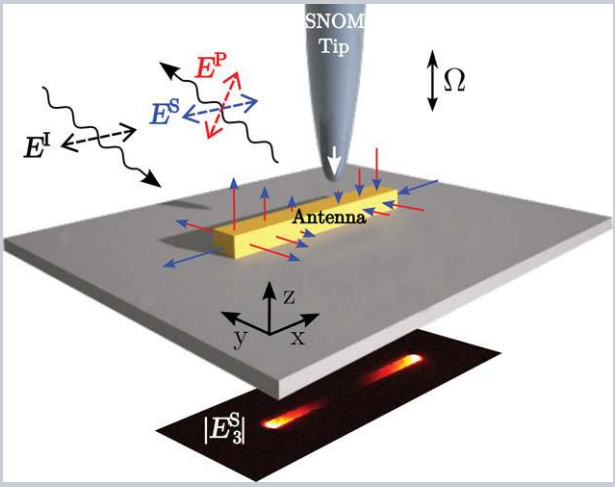

ORIGINAL PAPER

Mapping the near fields of plasmonic nanoantennas by scattering-type scanning near-field optical microscopy

Tomáš Neuman[1,2], Pablo Alonso-González[3], Aitzol Garcia-Etxarri[1], Martin Schnell[3], Rainer Hillenbrand[3], and Javier Aizpurua[1,*]

1. Introduction

Plasmonic nanoantennas are fundamental metallic systems that enable the localization and enhancement of electromagnetic radiation at subwavelength dimensions. These effects arise due to the excitation of a coherent oscillation of the metal's conduction electrons at the nanoantenna surface, the so-called surface plasmons [1–3]. The ability to localize light in the nanoscale opens the path to control optical electromagnetic fields beyond the diffraction limit. Optical nanofocusing has helped to improve the performance and resolution of field-enhanced spectroscopy [4] and microscopy [5]. Moreover, it has enabled key advances in a variety of technologies, such as in active control of optical signals [6, 7], biosensing [8, 9], medical therapies [10], photovoltaics [11] or optoelectronics [12], among others. The evaluation and mapping of local fields induced in optical nanoantennas is a challenging experimental task. Different techniques compete in the race for improving subwavelength resolution [13]. High-resolution energy-filtered electron energy loss spectroscopy (EELS), for instance, can successfully map the projection of the local density of states (LDOS) of a nanostructure by probing the fields with high-energy swift electrons that provide an impulsive excitation to the entire structure [14, 15]. However, this technique does not deliver amplitude- and phase-resolved maps, which are highly valuable for identifying the structure of an electromagnetic mode. Based on a different working principle, aperture-scanning near-field optical microscopy (a-SNOM) has also provided highly resolved maps of electric and magnetic fields in the 50 nm resolution range with use of metal-coated dielectric tips that guide and collect the

[1] Centro de Fisica de Materiales CSIC-UPV/EHU and Donostia International Physics Center DIPC, Paseo Manuel de Lardizabal 5, 20018 Donostia-San Sebastián, Spain
[2] CEITEC BUT, Brno University of Technology, Technická 10, 616 00, Brno, Czech Republic
[3] Nanooptics Laboratory, CIC nanoGUNE and UPV/EHU, 20018 Donostia-San Sebastián, Spain and IKERBASQUE, Basque Foundation for Science, 48011 Bilbao, Spain
*Corresponding author: e-mail: aizpurua@ehu.es

illumination to and from the sample structure [16]. Most of these techniques, however, probe the intensity of local field components, whereas a complete characterization of the full polarization state of the near fields of an antenna requires information on their amplitude and phase [17].

A promising approach to access the full polarization state of the near field around an antenna is scattering-type scanning near-field optical microscopy (s-SNOM) [18–29]. In s-SNOM, a scanning tip acts as a scatterer that transfers the near field induced in the vicinity of a nanoantenna to the far field, where it can be collected by a detector. Two main modes of operation can be identified depending on the strength of the interaction between the tip and the antenna. When material properties and spectroscopic information of the sample are required, strongly scattering (metallic) tips are used. These tips interact with the sample via their image charge [30–32], allowing for the identification of the dielectric properties of the sample underneath, thus providing *in situ* material contrast [33, 34]. However, when information on the near-field distribution around a nanoantenna is desired, a weakly scattering (dielectric) tip is needed to access this near field without distortion [18, 20, 21, 25, 29, 35, 36]. This technique was first introduced to access the amplitude and phase of plasmonic near fields in gold nanodisk antennas [18]. Nevertheless, the actual relationship between the local field components induced around the nanoantenna and the signal detected in the far field (at position $\mathbf{r}_{\mathrm{det}}$) is usually not straightforward [35, 37, 38]. In most of the previous studies, the signal detected in s-SNOM was considered to be directly proportional to the near-field vector at the position of the probing tip, thus showing a one-to-one correspondence between the components of the scattered far field responsible for the signal and the corresponding components of the antenna's near field (E_x, E_y, E_z) at each point. As we will see in this work, this description is incomplete, and a more accurate model that accounts for the multiple-scattering process between tip and antenna needs to be considered for an exact interpretation of the near-field maps.

A schematic of the scattering off a tip and a nanoantenna sample in a typical s-SNOM configuration is shown in Fig. 1. An incident field $\mathbf{E}^{\mathrm{I}}$ interacts with an antenna exciting local fields in its proximity. A weakly interacting tip, located at a particular local position, scatters light which is detected interferometrically, obtaining its amplitude and phase. One improvement of the s-SNOM technique involves the analysis of light polarized in a direction perpendicular to the polarization of the incident radiation, the so-called crossed-polarized detection configuration [20]. This helps improving the excitation and detection efficiencies, thus allowing one to identify higher-order modes of plasmonic nanoantennas [20, 21, 39].

As pointed out above, in a simplification to interpret the signal obtained in s-SNOM, the selection of *S*- or *P*-polarized scattered light (E^{S} and E^{P}, respectively) has been traditionally interpreted as a straightforward mapping of the corresponding in- and out-of-plane local near-field components, respectively, induced in the proximity of the plasmonic antenna at the tip position [18, 23, 24, 39–42].

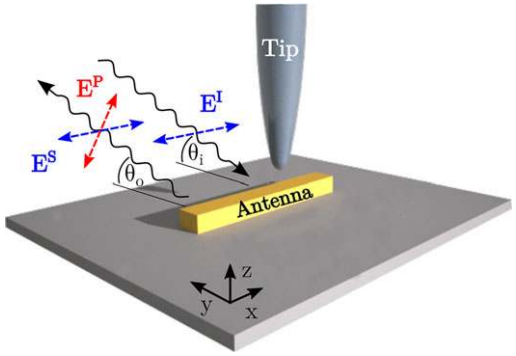

Figure 1 Schematics of the combined antenna–tip scattering in scattering-type scanning near-field optical microscopy (s-SNOM). In oblique-incidence mode, the incident wave vector $\mathbf{E}^{I}$ illuminates an antenna from the top at a certain angle θ_{i} with respect to the out-of-plane axis (z) with a direction of propagation (y) perpendicular to the antenna axis (x). The scattered field, $\mathbf{E}^{\mathrm{P}}$ or $\mathbf{E}^{\mathrm{S}}$, is collected by *P*- or *S*-polarized detectors, respectively, in the backscattered direction of propagation, at an angle of scattering $\theta_{\mathrm{o}} = \theta_{\mathrm{i}}$.

Following this assumption, and according to the schematics of Fig. 1, the *S*- and *P*-polarized fields detected by interferometric s-SNOM, E^{S} and E^{P}, respectively, have been often assigned in a simplified manner as $E^{\mathrm{S}} \propto E_x$ (in-plane) and $E^{\mathrm{P}} \propto E_z$ (out-of-plane). Using a more complete model that accounts for the multiple scattering of tip and antenna sample, here we show that E^{S} and E^{P} depend on a much more complex combination of the local near-field components (E_x, E_y and E_z), including linear and quadratic dependences. We apply our model to correctly interpret the s-SNOM near-field maps of single plasmonic dipolar and gap antennas. Nevertheless, our results are derived with generality and can be applied to interpret s-SNOM near-field maps of arbitrarily shaped plasmonic antennas.

2. Theoretical model

We describe in the following the theoretical model that accounts for the multiple scattering produced between probing tip and antenna sample, using the reciprocity theorem of electromagnetic fields. This approach allows for a correct interpretation of s-SNOM maps in terms of a combination of complex-valued components of the local near field around the plasmonic antenna, thus amending previous simplified interpretations.

2.1. General approach to antenna–tip scattering

The description of the s-SNOM signal yields a direct scattering problem determined by two scatterers: the tip (T) and the sample antenna (A). In the following, we treat the scattering problem with generality within the formalism of the linear response based on the dyadic Green's function.

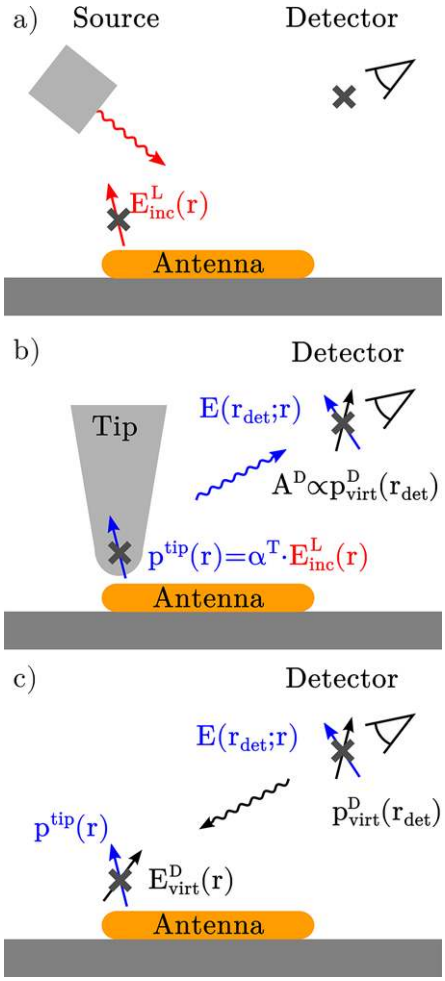

Figure 2 Schematics of the scattering model to obtain the s-SNOM signal based on the reciprocity theorem. (a) An incident field produces a local field, $\mathbf{E}^{L}_{inc}(\mathbf{r})$, in the proximity of the antenna at position $\mathbf{r}$. (b) A tip of polarizability α^T is located in the proximity of the antenna, producing a dipole momentum $\mathbf{p}^{tip}(\mathbf{r})$. This dipole scatters off the field in the proximity of the antenna to the detector, $\mathbf{E}(\mathbf{r}_{det};\mathbf{r})$, where a polarizer along a particular direction, $\mathbf{A}^D$, selects the polarization of the signal detected. (c) Together with the tip dipole and the field scattered at the detector, the virtual dipole at the detector (parallel to the detection polarization, $\mathbf{p}^D_{virt}(\mathbf{r}_{det}) \propto \mathbf{A}^D$), and the corresponding virtual near field, $\mathbf{E}^D_{virt}(\mathbf{r})$, form the four elements to apply the reciprocity theorem.

As depicted in the schematics of Fig. 2(a), we first define the local near field around the antenna, $\mathbf{E}^L_{inc}(\mathbf{r})$, at a position $\mathbf{r}$, excited by the incident laser illumination employed in the experiment:

$$\mathbf{E}^L_{inc}(\mathbf{r}) = \mathbf{E}^A(\mathbf{r}) + \mathbf{E}^I(\mathbf{r}), \tag{1}$$

which consists of the contribution of the incident field $\mathbf{E}^I$ plus the near field produced by the scattering from the antenna $\mathbf{E}^A$, in the absence of the tip.

We can make a first approximation and consider that the s-SNOM tip can be represented by an equivalent point-like scatterer with polarizability α^T, given by a diagonal tensor:

$$\boldsymbol{\alpha}^T \approx \begin{pmatrix} \alpha^T_x & 0 & 0 \\ 0 & \alpha^T_y & 0 \\ 0 & 0 & \alpha^T_z \end{pmatrix}, \tag{2}$$

where α^T_x, α^T_y and α^T_z are the components of the tip polarizability tensor along each of the Cartesian coordinates x, y and z. All the components of this tensor are indeed important and, typically, the component along the direction of elongation of the tip, α^T_z, is usually slightly larger than the transverse ones, but comparable in magnitude. The assumption of a point-like dipole to describe the tip is particularly suitable considering the small size of the tip apex compared to that of the infrared plasmonic antennas, as well as its relative smaller polarizability. However, this assumption might impose limitations in the description when mapping extended two-dimensional antenna structures where additional areas of the tip, beyond its apex, might influence the scattering process.

When the tip is placed in the vicinity of the antenna, as depicted in the schematics of Fig. 2(b), the near field around the antenna, $\mathbf{E}^L_{inc}(\mathbf{r})$, induces a dipole moment in the tip, $\mathbf{p}^{tip}(\mathbf{r})$, given by

$$\mathbf{p}^{tip}(\mathbf{r}) = \boldsymbol{\alpha}^T \cdot \mathbf{E}^L_{inc}(\mathbf{r}). \tag{3}$$

The polarized tip in turn radiates from the vicinity of the antenna the field $\mathbf{E}(\mathbf{r}_{ext})$ out to a general distant position $\mathbf{r}_{ext}$. To express the field produced by a dipole, we formally define the antenna dyadic Green's function $\mathcal{G}(\mathbf{r}', \mathbf{r})$ as the propagator that generates a field distribution at a position $\mathbf{r}'$ by a point-source dipole located at $\mathbf{r}$, precisely considering the electromagnetic environment, i.e. the antenna, the substrate and the illumination and detection optics. The generality of this definition makes this formalism a valuable tool for the analysis of generic experimental conditions of illumination and detection. Within the weak-interaction limit, where the tip can be treated as a weakly polarizable object, the scattering by the tip to the position of the detector $\mathbf{r}_{det}$ can be expressed in terms of the Green's function as

$$\mathbf{E}(\mathbf{r}_{det};\mathbf{r}) = \frac{k_0^2}{\varepsilon_0} \mathcal{G}(\mathbf{r}_{det}, \mathbf{r}) \cdot \boldsymbol{\alpha}^T \cdot \mathbf{E}^L_{inc}(\mathbf{r}), \tag{4}$$

where we note that the scattered field is evaluated at an external position $\mathbf{r}_{det}$, while being also implicitly dependent on the near-field position of the tip $\mathbf{r}$.

The expression in Eq. (4) is equivalent to a multiple-scattering description of the tip–sample interaction, restricted to the first-order scattering off the tip, as detailed in the Supp. Inf. However, in a simplification of Eq. (4), the multiple scattering between tip and sample, included in the Green's function, is usually not considered, and the scattered far field is assumed to be the result of the

direct propagation of light from the tip dipole (i.e. vacuum Green's function, $\mathscr{G}_o$, instead of $\mathscr{G}$) [18, 23, 24, 39–42]:

$$\mathbf{E}(\mathbf{r}_{\rm det};\mathbf{r}) \propto \mathscr{G}_o(\mathbf{r}_{\rm det}.\mathbf{r}) \cdot \alpha^{\rm T} \cdot \mathbf{E}^{\rm L}_{\rm inc}(\mathbf{r}). \quad (5)$$

This expression assumes that the transfer of the antenna near field, $\mathbf{E}^{\rm L}_{\rm inc}(\mathbf{r})$, into the s-SNOM signal ($E^{\rm S}$, $E^{\rm P}$), can be described in Cartesian coordinates (Fig. 1) as

$$E^{\rm S} \propto \alpha^{\rm T}_S \cdot E_x, \quad (6)$$

$$E^{\rm P} \propto \alpha^{\rm T}_P \cdot E_z, \quad (7)$$

where $\alpha^{\rm T}_S$ and $\alpha^{\rm T}_P$ are the polarizabilities of the tip along the x and z directions, respectively. This assumption can explain many features of near-field maps, but it can also lead to misinterpretation, as we will show in the following sections. A formalism that accounts for the antenna–tip scattering in a more complete manner is thus needed.

2.2. Polarization-resolved s-SNOM maps: interpretation via the reciprocity theorem

We describe in this section the derivation of a more complete formalism to obtain the scattered far field from the antenna–tip system. With use of the reciprocity theorem of electromagnetism, the multiple scattering by the antenna–tip system can be properly accounted for (up to the first-order scattering off the tip), providing a different and more complete interpretation of the near-field maps.

The signal measured by s-SNOM is proportional to the amplitude of the field scattered from the antenna–tip system (before demodulation). The information on the amplitude of the scattered field is obtained thanks to the interferometric detection scheme. By locating a linear polarizer (analyzer) in front of the detector, it is possible to measure a specific component of the far field scattered by the tip–antenna system [20, 22, 25, 29]. Mathematically, the action of the polarizer on the scattered field can be represented as a scalar product between the complex-valued amplitude of the scattered field in Eq. (4), $\mathbf{E}(\mathbf{r}_{\rm det};\mathbf{r})$, and a unit vector in the direction of the polarizer axis, $\mathbf{A}^{\rm D}$, which we identify as proportional to a *virtual* point dipole at the position of the detector, $\mathbf{A}^{\rm D} \propto \mathbf{p}^{\rm D}_{\rm virt}(\mathbf{r}_{\rm det})$, as schematically depicted in Fig. 2(b). The projection of the radiated field at the detector, $E^{\rm det}$, can thus be expressed as

$$E^{\rm det}(\mathbf{r}) = \mathbf{A}^{\rm D} \cdot \mathbf{E}(\mathbf{r}_{\rm det};\mathbf{r}) \propto \mathbf{p}^{\rm D}_{\rm virt}(\mathbf{r}_{\rm det}) \cdot \mathbf{E}(\mathbf{r}_{\rm det};\mathbf{r}). \quad (8)$$

If we now apply the reciprocity theorem to the pair of point dipoles at the local position of the antenna, $\mathbf{r}$, and at the detector, $\mathbf{r}_{\rm det}$ [37, 43, 44], we can express the following relationship:

$$\mathbf{E}(\mathbf{r}_{\rm det};\mathbf{r}) \cdot \mathbf{p}^{\rm D}_{\rm virt}(\mathbf{r}_{\rm det}) = \mathbf{E}^{\rm D}_{\rm virt}(\mathbf{r}) \cdot \mathbf{p}^{\rm tip}(\mathbf{r}), \quad (9)$$

where $\mathbf{E}^{\rm D}_{\rm virt}(\mathbf{r})$ is the virtual local near field produced in the vicinity of the nanoantenna at the tip position, $\mathbf{r}$, generated by the virtual point dipole, $\mathbf{p}^{\rm D}_{\rm virt}(\mathbf{r}_{\rm det})$, located at the detector position, $\mathbf{r}_{\rm det}$, oriented along the direction of the analyzer, as schematically depicted in Fig. 2(c). Such definition of the virtual near field $\mathbf{E}^{\rm D}_{\rm virt}$ fully accounts for the influence of the detection optics, through a backward propagation scheme. Note that $\mathbf{E}^{\rm D}_{\rm virt}$ is indeed independent of the amplitude of the real incident field, $\mathbf{E}^{\rm I}$, since it is a result of a suitably normalized virtual source.

The left-hand side of Eq. (9) indeed accounts for the polarization-resolved field at the detector, $E^{\rm det}(\mathbf{r}) \propto \mathbf{E}(\mathbf{r}_{\rm det};\mathbf{r}) \cdot \mathbf{p}^{\rm D}_{\rm virt}(\mathbf{r}_{\rm det})$, which gives the s-SNOM signal (before demodulation). Following the reciprocity theorem in Eq. (9), we can thus express the detected projection of the scattered field in terms of (i) the virtual local near field around the antenna excited by a point dipole located at the detector position and oriented along the detection polarization axis and (ii) the real local near field excited in the antenna by the incoming laser light, as

$$E^{\rm det}(\mathbf{r}) \sim \mathbf{E}^{\rm D}_{\rm virt}(\mathbf{r}) \cdot \boldsymbol{\alpha}^{\rm T} \cdot \mathbf{E}^{\rm L}_{\rm inc}(\mathbf{r}), \quad (10)$$

where $\mathbf{r}$ is the tip position in the vicinity of the nanoantenna.

Equation (10) is the fundamental result of this paper, and its application provides new insights to connect the polarization-resolved s-SNOM signal with the local near-field components produced at the antenna by the incident and virtual fields [27]. This compact expression is radically different to the commonly assumed relationship between the near field and the scattered far field, expressed in Eq. (5).

As depicted in Fig. 1, we are mostly interested in configurations of the detection polarizer along the S or P directions; therefore, we identify the local virtual fields for these polarizations as $\mathbf{E}^{\rm D=S}_{\rm virt}$ and $\mathbf{E}^{\rm D=P}_{\rm virt}$, respectively.

Following Eq. (10), the expressions of the scattered field for each polarization, $E^{\rm det=S}$ and $E^{\rm det=P}$, can be related to the x, y and z components of the local near-field vectors ($E^{\rm L}_{\rm inc,x}$, $E^{\rm L}_{\rm inc,y}$, $E^{\rm L}_{\rm inc,z}$) and ($E^{\rm D}_{\rm virt,x}$, $E^{\rm D}_{\rm virt,y}$, $E^{\rm D}_{\rm virt,z}$), where L refers to a specific polarization state of the incident laser light and D to the polarization of the detected light (both L and D can thus be S or P), as well as to the diagonal components of the tip polarizability ($\alpha^{\rm T}_x$, $\alpha^{\rm T}_y$, $\alpha^{\rm T}_z$):

$$E^{\rm S}(\mathbf{r}) \sim \mathbf{E}^{\rm S}_{\rm virt}(\mathbf{r}) \cdot \boldsymbol{\alpha}^{\rm T} \cdot \mathbf{E}^{\rm L}_{\rm inc}(\mathbf{r}) = E^{\rm S}_{{\rm virt},x}(\mathbf{r})\alpha^{\rm T}_x E^{\rm L}_{{\rm inc},x}(\mathbf{r}) + E^{\rm S}_{{\rm virt},y}(\mathbf{r})\alpha^{\rm T}_y E^{\rm L}_{{\rm inc},y}(\mathbf{r}) + E^{\rm S}_{{\rm virt},z}(\mathbf{r})\alpha^{\rm T}_z E^{\rm L}_{{\rm inc},z}(\mathbf{r}), \quad (11)$$

$$E^{\rm P}(\mathbf{r}) \sim \mathbf{E}^{\rm P}_{\rm virt}(\mathbf{r}) \cdot \boldsymbol{\alpha}^{\rm T} \cdot \mathbf{E}^{\rm L}_{\rm inc}(\mathbf{r}) = E^{\rm P}_{{\rm virt},x}(\mathbf{r})\alpha^{\rm T}_x E^{\rm L}_{{\rm inc},x}(\mathbf{r}) + E^{\rm P}_{{\rm virt},y}(\mathbf{r})\alpha^{\rm T}_y E^{\rm L}_{{\rm inc},y}(\mathbf{r}) + E^{\rm P}_{{\rm virt},z}(\mathbf{r})\alpha^{\rm T}_z E^{\rm L}_{{\rm inc},z}(\mathbf{r}). \quad (12)$$

Equations (11) and (12) provide a general and straightforward way to relate the polarization-resolved scattered far field with the local near field induced at the nanoantenna at the position of the tip $\mathbf{r}$. According to this relationship, the s-SNOM signal can be correctly predicted if one calculates (i) the local near-field distribution induced in an antenna

by the real incident light $\mathbf{E}^{\mathrm{L}}_{\mathrm{inc}}$ and (ii) the virtual field $\mathbf{E}^{\mathrm{D}}_{\mathrm{virt}}$ excited by a dipolar source located at the detector oriented in the direction of its polarization axis. Following Eqs. (11) and (12), these two local fields are tensorially weighted by the components of the tip polarizability. Therefore, to obtain the polarized scattered far field only requires a numerical solution of the local near-field components produced by the incident and virtual radiations. This can be easily implemented for any arbitrarily shaped antenna with use of conventional solvers of Maxwell's equations, as we will show in the next sections.

2.3. Combination of near-field components in s-SNOM maps: parallel illumination and backscattering detection

The local near field $\mathbf{E}^{\mathrm{L}}_{\mathrm{inc}}(\mathbf{r})$ produced in the vicinity of the antenna, which is the magnitude we want to map, is the response of the antenna to a particular incident field polarized along a direction (L being either S or P). In our case, we will consider that the incident field is polarized along the antenna axis x, i.e. it can be considered as an S-polarized incident plane wave; therefore, $\mathbf{E}^{\mathrm{L}}_{\mathrm{inc}} = \mathbf{E}^{\mathrm{S}}_{\mathrm{inc}}$. We denote the tip position-dependent components of this local near field as

$$E^{\mathrm{L}}_{\mathrm{inc},x}(\mathbf{r}) = E^{\mathrm{S}}_{\mathrm{inc},x}(\mathbf{r}) = f_x \cdot E^{\mathrm{I}} = E_x, \tag{13}$$

$$E^{\mathrm{L}}_{\mathrm{inc},y}(\mathbf{r}) = E^{\mathrm{S}}_{\mathrm{inc},y}(\mathbf{r}) = f_y \cdot E^{\mathrm{I}} = E_y, \tag{14}$$

$$E^{\mathrm{L}}_{\mathrm{inc},z}(\mathbf{r}) = E^{\mathrm{S}}_{\mathrm{inc},z}(\mathbf{r}) = f_z \cdot E^{\mathrm{I}} = E_z, \tag{15}$$

where we define the components of the local field enhancement, f_x, f_y and f_z, as the ratio between the corresponding local near-field component and the incident field amplitude. In the case of P-polarized incident radiation, we would denote the local near field around the antenna as $\mathbf{E}^{\mathrm{L}}_{\mathrm{inc}} = \mathbf{E}^{\mathrm{P}}_{\mathrm{inc}}$.

In a backscattering s-SNOM configuration scheme, the incident and backdetection directions are equivalent; thus, we can relate the local near fields produced at the antenna by the polarized virtual fields ($\mathbf{E}^{\mathrm{S}}_{\mathrm{virt}}$ and $\mathbf{E}^{\mathrm{P}}_{\mathrm{virt}}$) with those produced by the incident laser radiation (with the same polarization):

$$\mathbf{E}^{\mathrm{S}}_{\mathrm{virt}} \propto \mathbf{E}^{\mathrm{S}}_{\mathrm{inc}}/E^{\mathrm{I}} = \mathbf{f}^{\mathrm{S}}, \tag{16}$$

$$\mathbf{E}^{\mathrm{P}}_{\mathrm{virt}} \propto \mathbf{E}^{\mathrm{P}}_{\mathrm{inc}}/E^{\mathrm{I}} = \mathbf{f}^{\mathrm{P}}, \tag{17}$$

where $\mathbf{f}^{\mathrm{S}}$ and $\mathbf{f}^{\mathrm{P}}$ are the local near-field enhancement vectors produced by S- and P-polarized incident light, respectively.

Following this notation, the signals measured when selecting the S- and P-polarized components of the scattered light can be further simplified as

$$\begin{aligned} E^{\mathrm{S}}(\mathbf{r}) &\sim \left(\mathbf{E}^{\mathrm{S}}_{\mathrm{inc}}(\mathbf{r})/E^{\mathrm{I}}\right) \cdot \boldsymbol{\alpha}^{T} \cdot \mathbf{E}^{\mathrm{S}}_{\mathrm{inc}}(\mathbf{r}) \\ &= \mathbf{f}^{\mathrm{S}}(\mathbf{r}) \cdot \boldsymbol{\alpha}^{T} \cdot \mathbf{f}^{\mathrm{S}}(\mathbf{r}) \cdot E^{\mathrm{I}}, \end{aligned} \tag{18}$$

$$\begin{aligned} E^{\mathrm{P}}(\mathbf{r}) &\sim \left(\mathbf{E}^{\mathrm{P}}_{\mathrm{inc}}(\mathbf{r})/E^{\mathrm{I}}\right) \cdot \boldsymbol{\alpha}^{T} \cdot \mathbf{E}^{\mathrm{S}}_{\mathrm{inc}}(\mathbf{r}) \\ &= \mathbf{f}^{\mathrm{P}}(\mathbf{r}) \cdot \boldsymbol{\alpha}^{T} \cdot \mathbf{f}^{\mathrm{S}}(\mathbf{r}) \cdot E^{\mathrm{I}}. \end{aligned} \tag{19}$$

Equations (18) and (19) are novel expressions that describe the s-SNOM signals in a different way to that commonly treated to date [20, 23, 24, 39–41]. The signal at the detector is expressed in terms of a product of the vectors of local field enhancement produced by the illumination from (i) the real source and (ii) the virtual source located at the detector, with the same polarization as the detection scheme. Furthermore, the product of local field enhancements is weighted by the corresponding components of the tip polarizability tensor.

We now develop the expressions above for the case of a plasmonic antenna strongly polarizable along one axis, x, as depicted in Fig. 1. We consider the setup shown in the figure, with S-polarized light incident at an angle $\theta_{\mathrm{o}} = 45^{\circ}$, and a backscattering detection scheme. The virtual excitation of the antenna with polarization perpendicular to its axis produces a very weak response of the local near-field enhancement at the antenna, $\mathbf{f}^{\mathrm{P}}$, since this polarization is perpendicular to the antenna's main axis. Therefore, effectively, we can assume the local near field to be equal to the P-polarized incident field, and set $\mathbf{f}^{\mathrm{P}} \propto (0, -1, 1)$ in Eq. (19), since the incoming light is barely modified by the antenna for this polarization.

Considering all the above, the expressions for the position-dependent S- and P-polarized far-field components of the scattered field, i.e. the s-SNOM signals, $E^{\mathrm{P}}(\mathbf{r}) = E^{\mathrm{P}}$ and $E^{\mathrm{S}}(\mathbf{r}) = E^{\mathrm{S}}$, of a dipolar antenna excited along its polarization axis x can be expressed in terms of the near-field components (E_x, E_y and E_z) produced by the incoming light around the antenna [or equivalently in terms of the field enhancement components (f_x, f_y, f_z)] as

$$\begin{aligned} E^{\mathrm{S}} &\propto \frac{\left(\alpha^{\mathrm{T}}_x E_x^2 + \alpha^{\mathrm{T}}_y E_y^2 + \alpha^{\mathrm{T}}_z E_z^2\right)}{E^{\mathrm{I}}} \\ &= \left(\alpha^{\mathrm{T}}_x f_x^2 + \alpha^{\mathrm{T}}_y f_y^2 + \alpha^{\mathrm{T}}_z f_z^2\right) \cdot E^{\mathrm{I}} \end{aligned} \tag{20}$$

and

$$E^{\mathrm{P}} \propto \left(\alpha^{\mathrm{T}}_z E_z - \alpha^{\mathrm{T}}_y E_y\right) = \left(\alpha^{\mathrm{T}}_z f_z - \alpha^{\mathrm{T}}_y f_y\right) \cdot E^{\mathrm{I}}. \tag{21}$$

A striking consequence of Eqs. (20) and (21) is that the scattered field obtained with the P-polarized detection scheme provides a signal which is proportional to a linear combination of the y and z components of the local near-field enhancement induced around the antenna, f_y and f_z, weighted by the respective components of the polarizability tensor of the tip, α^{T}_y and α^{T}_z. However, the S-polarized detection scheme (detection polarization parallel to the polarization of the incident field) provides a signal which depends quadratically on the three components of the local field enhancement, f_x^2, f_y^2 and f_z^2, weighted by the corresponding components of the tip polarizability tensor [see Eq. (20)].

The linear dependence on the local field for P-polarized detection is determined by the single involvement of the antenna in the signal formation. The antenna solely enhances the near field and induces the dipole moment of the tip, which directly radiates to the detector. Due to the particular arrangement of the experiment, P-polarized scattering from the antenna is not allowed; therefore, the second scattering process from the antenna is forbidden. The quadratic dependence for the S-polarized detection, however, does involve a double role of the antenna: first the antenna interacts with the incoming field and produces a strong local near field that polarizes the tip, and then the emission of the tip to the far field is again mediated by the antenna, leading to a second enhancement of the resulting far-field amplitude. This so-called double scattering by the antenna is commonly present and exploited in field-enhanced spectroscopies, where the field enhancement produced is obtained by the double scattering of a variety of optical nanoantennas, such as in SERS or TERS [45–47]. In our case, however, the process is completely elastic[27].

In the following sections we demonstrate the significance of the theoretical results obtained in Eqs. (20) and (21) by comparing our theoretical predictions with experimental results obtained in s-SNOM for plasmonic nanoantennas. Before doing so, we properly describe and account for the demodulation scheme employed in experiments. In practice, an oscillating tip is employed in tapping mode to modulate the far-field signal. The detector is equipped with a lock-in amplifier and only higher harmonic tapping frequencies of the signal are recorded, generating two-dimensional near-field maps of the antennas when properly scanned.

2.4. Demodulation of the signal

The modulation of the distance between the antenna and tip produces the corresponding modulation of the scattered far-field signal $\mathbf{E}^{\mathrm{det}}(\mathbf{r})$. The modulation of the separation distance can be done by sinusoidally modifying the position of the tip $\mathbf{r}$ at a frequency Ω in the vertical direction as $\mathbf{r}(t) = \mathbf{r}_{\mathrm{T}}^{\parallel} + \hat{\mathbf{z}}[z_{\mathrm{min}}(\mathbf{r}_{\mathrm{T}}^{\parallel}) + \Delta + \Delta\cos(\Omega t)]$. Here, $\mathbf{r}_{\mathrm{T}}^{\parallel}$ denotes the lateral position of the tip which only slowly varies with time, Δ is the amplitude of the tip oscillation and $z_{\mathrm{min}}(\mathbf{r}_{\mathrm{T}}^{\parallel})$ represents the lowest point of the tip oscillation. The resulting s-SNOM image is then a function of the lateral tip position $\mathbf{r}_{\mathrm{T}}^{\parallel}$ after time Fourier transforming the signal at each point.

The n^{th}-order demodulated signal, $(E^{\mathrm{det}})_n \equiv E_n^{\mathrm{det}}$, can be obtained by Fourier transforming $E^{\mathrm{det}}(\mathbf{r})$, according to

$$(E^{\mathrm{det}})_n(\mathbf{r}_{\mathrm{T}}^{\parallel}) = \int E^{\mathrm{det}}(\mathbf{r})\cos(n\Omega t)\mathrm{d}t. \qquad (22)$$

The demodulation of the signal using Eq. (22) together with the harmonic oscillation of the tip pertains only to the signal coming from the mutual interaction between the antenna and the tip.

The idealized description of the tip as a harmonically oscillating object might fail in practice due to several experimental limitations such as the anharmonicity of the tip oscillation [38, 48] or a varying polarizability of the tip with the distance from the antenna sample (due to the finite size of the tip). In order to account effectively for the phenomenon of anharmonicity, we implement for the third demodulation order the following effective tip oscillation [38]:

$$\mathbf{r} = \mathbf{r}_{\mathrm{T}}^{\parallel} + \hat{\mathbf{z}}\left\{z_{\mathrm{min}}(\mathbf{r}_{\mathrm{T}}^{\parallel}) + \Delta + \frac{\Delta}{(\Delta+\delta)}\left[\Delta\cos(\Omega t) + \delta\cos(3\Omega t)\right]\right\}, \qquad (23)$$

where δ represents an anharmonicity parameter. The experimental determination of the level of tip anharmonicity is highly challenging; we thus use δ as a free parameter which we adjust to resemble the experimental situation.

Generally speaking, the demodulation of the signal introduces certain effects to the images connected with the spatial variation of the measured signal. Rapid variations of the non-demodulated signal in the vertical direction produce larger values of the higher-order demodulated signal. On the other hand, a constant signal or a signal slowly varying in the vertical direction will contribute only negligibly to the resulting demodulated image. Such effects lead to a sharpening of the higher-harmonic near-field images close to the areas of rapidly varying fields. In the next section we will see that such areas can be found close to the antenna extremities. Since complex numbers are demodulated during the procedure, their phase also undergoes transformation. One significant effect of this phase transformation is connected with a change of sign, which can completely reverse the phase image between different demodulation orders. Therefore, it is not possible to provide a straightforward and absolute connection between the phase of the near fields and the recorded higher-order phase images. The relative phase within the higher-order images, however, provides an accurate picture of the non-demodulated signal, especially when the anharmonicity is introduced. The anharmonicity itself has the effect of smearing out the sharpening of the image amplitude and recovers the first-order demodulated image for high values of the parameter δ. Nevertheless, the main trends of the polarization-resolved s-SNOM signal of plasmonic nanoantennas are given by Eqs. (21) and (20), as we detail in the next sections.

3. Near-field maps of single linear antennas

We first apply the theoretical model developed in the previous sections to single rod-like linear antennas. The full theory that accounts for the combination of near-field components will prove essential for a correct interpretation of the s-SNOM experimental images. The calculation of the local fields induced by the incoming light and by the virtual fields is performed for the antennas deposited on the

substrate by solving Maxwell equations within the finite-difference time-domain method (FDTD) [49].

3.1. Local near-field components

The illumination of the single antennas (3.8 μm long and 150 nm wide resonant at wavelength 11.06 μm) follows a scheme such as the one illustrated in Fig. 1. *S*-polarized light (along the x axis) polarizes the antenna and induces a distribution of local near-field components in the xy plane on top of the antenna, $E_i(x, y)$ with $i = x, y, z$. In Fig. 3, we plot the calculated amplitude and phase of the three components of the near field for a model antenna under such illumination.

The amplitude of the in-plane component along the antenna axis, $|E_x|$ [Fig. 3(a)], shows the typical dipolar pattern with field expelled out of the poles of the induced antenna dipole at each side of the antenna. The relative phase, φ_x, remains the same at both sides since the near fields point in the same direction at both poles. The in-plane component in the perpendicular direction, $|E_y|$ [Fig. 3(b)], also shows a near field expelled towards the sides of the poles of the induced antenna dipole with a phase shift, φ_y, of π both along the antenna axis as well as in the perpendicular direction. Finally, the amplitude of the out-of-plane component, $|E_z|$ [Fig. 3(c)], shows a noticeable enhancement on top of the antenna increasing in value from the center towards its edges. A phase shift, φ_z, of π also identifies clearly the change in sign of the field induced at both sides of the antenna.

In the next section we will show that the signal measured by s-SNOM can be related to the components of the antenna near field via the theoretical model developed above [Eqs. (20) and (21)].

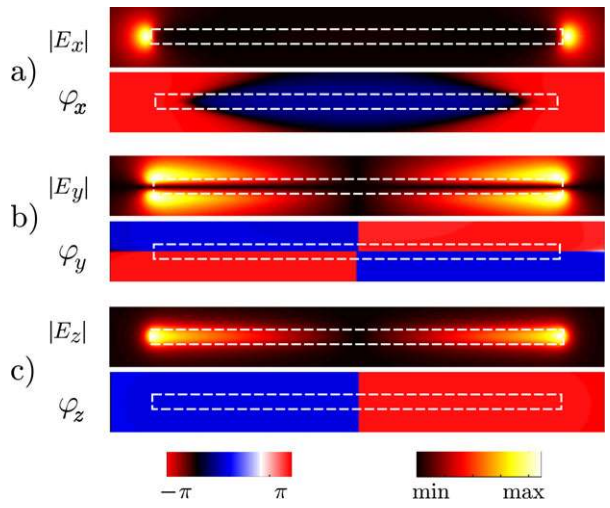

Figure 3 Calculated local near-field components (normalized amplitude $|E|$, top, and relative phase φ offset to zero, bottom) induced on a plane 30 nm on top of a single Au nanoantenna when it is illuminated by light linearly polarized along the antenna axis (x). (a) x component of the field enhancement E_x, (b) y component E_y and (c) z component E_z. The antenna length is 3.8 μm.

3.2. Interpretation of near-field maps within the theoretical model

In this section we will show the amplitude and phase of the s-SNOM signal given by the scattering off the tip in the vicinity of infrared plasmonic linear antennas. In order to test our model, we compare the signals obtained in the framework of the more complete theoretical model with the experimental s-SNOM images. This microscopic technique, based on atomic force microscopy (AFM), allows for simultaneous detection of optical signal and sample topography. For the experiments we used the neaSNOM from neaspec GmbH (see schematics of the setup in Supp. Inf.), where the nanoantenna and a conventional AFM Si tip are illuminated from the side (at an angle of about 45° with respect to the surface normal) with a focused CO_2 laser operating at a wavelength of 11.06 μm. The polarization of the illuminating beam is set to be parallel to the antenna axis x (as depicted in Fig. 1). The s-SNOM is operated in the so-called *backscattering* mode of operation [21,27,36,41]. Pseudo-heterodyne interferometry is utilized for simultaneous detection of amplitude and phase of the optical signal. Background contributions from the tip and nanoantenna are suppressed by vertical oscillation of the tip with respect to the nanoantenna at a tapping frequency $\Omega = 300$ kHz (tapping mode AFM) [30]. The n^{th}-order harmonic demodulation of the detected signal E_n provides information on the near field in the proximity of the nanoantenna. Two infrared polarizers are located in front of the detector in the interferometer to select *P*- and *S*-polarized scattered fields, which provide the signals E_n^{P} and E_n^{S}, respectively, and we have a 45° polarizer in the reference arm. The third order of demodulation ($n = 3$) is used here to obtain the near-field maps of the nanoantennas.

With use of this setup, we first analyze single dipolar linear plasmonic nanoantennas on a CaF_2 substrate (gap nanoantennas are analyzed in the next sections). The dimensions of the nanoantennas are chosen to be in resonance with the illuminating wavelength at 11.06 μm, which corresponds to an antenna length of 3.8 μm. The width of the antenna is 150 nm. The topography of the linear nanoantenna used in the experiments is shown in Fig. 4(a), left. In Fig. 4(b) and (c) we show the experimental images of amplitude $|E_3|$ (top) and phase φ_3 (bottom) signals of a single metallic nanoantenna with use of *S*- and *P*-polarized detection, respectively (left-hand-side panels). The dipolar pattern of the antenna near field is identified in *P*-polarized detection as a strong amplitude signal $|E_3^{\text{P}}|$ at both extremities of the antenna and a phase shift φ_3^{P} of π between both antenna sides [Fig. 4(c), left]. These amplitude and phase distributions along the antenna axis have been associated to the direct mapping of the out-of-plane component, E_z, of the near field in a conventional interpretation of s-SNOM images. However, it is possible to identify the contribution

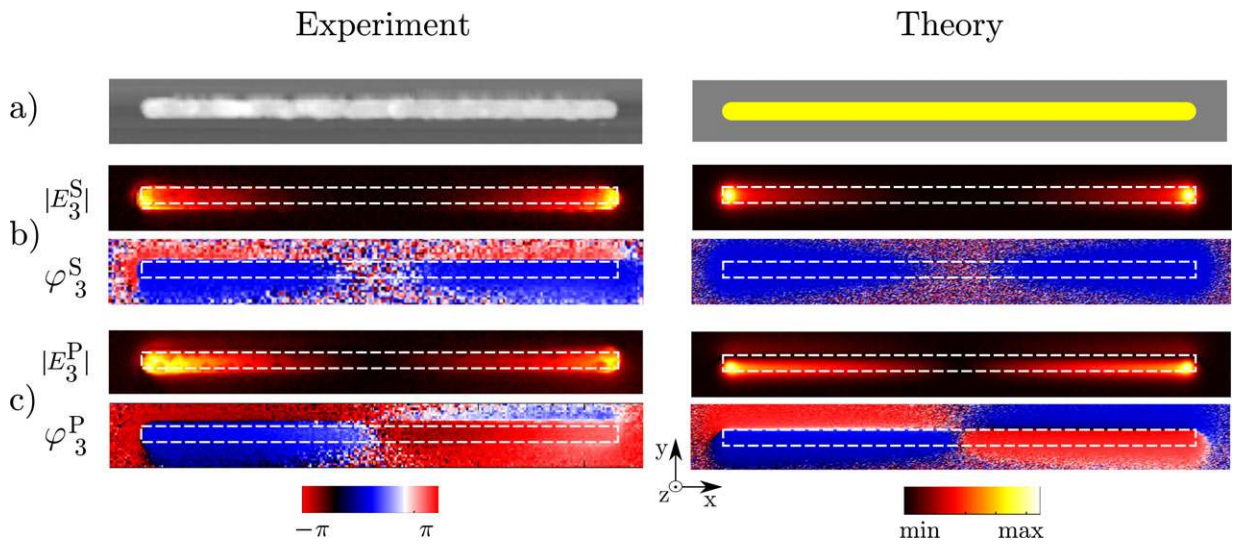

Figure 4 Comparison of experimental and theoretical s-SNOM images in a single Au antenna. (a) Topography (left) and schematics of the geometry used in the calculations of the local fields around the antenna (right). (b), (c) s-SNOM amplitude $|E_3|$ and phase φ_3 signals obtained with (b) *S*-polarized detection and (c) *P*-polarized detection. Experimental signals are displayed to the left and calculated amplitude $|E_3|$ and phase φ_3 of the demodulated scattered far field from the antenna to the right in both cases. The demodulated scattered far-field maps are obtained from the evaluation of the expressions in Eqs. (18) and (19). Anharmonicity and noise have also been included as described in the text. Antenna length is 3.8 μm. The theoretical images are calculated assuming an effective tip radius of 30 nm, a tapping amplitude of $\Delta = 85$ nm and an anharmonicity parameter of $\delta = 0.05\Delta$.

of the transverse in-plane component, E_y (transverse direction crossing from the antenna surface to the substrate), particularly in the phase image, which departs from this interpretation. This phase jump of π in the y direction is noticeable in the experimental phase map of Fig. 4(c), bottom left, and points towards the influence of the y-component projection on the s-SNOM signal obtained with P polarization. In the area above the antenna the component E_z plays the dominant role. However, when the signal is detected in areas at the sides of the antenna, the component E_y overtakes the leading role causing the observed phase jump in the transverse direction. We will see below how the presence of different components, conveniently combined as introduced in our model, successfully interprets these features.

Even more striking results are observed when the S-polarized scattered field is detected ($|E_3^S|$). s-SNOM images obtained with S polarization cannot be explained as a simple projection of the in-plane near-field components, mapped in the far field via the tip radiation. The experimental amplitude signal, $|E_3^S|$ [Fig. 4(b), top left], shows a dipolar pattern with large intensity that extends on top of the metal. However, the phase distribution φ_3^S in Fig. 4(b), bottom left, indicates a zero phase shift between the antenna arms. The in-plane component of the local near field E_x [displayed in Fig. 3(a)] shows similarities with the observed phase distribution, but it fails to address the distribution of the experimental amplitude: the fields associated with the x component are expelled out of the antenna, as observed in Fig. 3(a); however, $|E_3^S|$ shows a substantial contribution of signal from positions on top of the antenna, pointing towards the influence of the E_z component in this signal. The full theoretical model is thus necessary to interpret the experimental images obtained with S polarization, as described below.

We calculate the demodulated signal (including the effect of anharmonicity) for both P- and S-polarized detections following the theoretical framework introduced in the previous sections [Eqs. (18), (19) and (23)]. The actual implementation of the numerical calculations for both polarizations is described in detail in Supp. Inf. We consider a demodulation order $n = 3$, as in the experiment, and an effective tip radius of 30 nm. For demodulation, the tapping amplitude of the tip is assumed to be $\Delta = 85$ nm and the anharmonicity parameter is adjusted to $\delta = 0.05\Delta$. The experimental signal suffers from background noise, which effectively prevents a reliable measurement of phase in areas of low signal intensity. To take this into account, a random signal generated with a normal distribution centered at zero and standard deviation equal to 1% of the signal amplitude maximum is added to the theoretically demodulated signal. The calculated near-field maps are shown at the right-hand side of Fig. 4(b) and (c) for S- and P-polarized detection, respectively.

For P-polarized detection [Fig. 4(c), right], the amplitude and phase from our model reproduce perfectly the experimental dipolar pattern of the antenna resonance, including the phase jump between the antenna surface and substrate in the y direction consistently with the assumed dependence of the signal on E_z and E_y in Eq. (21).

When the full theoretical analysis is applied to the S-polarized detection, the squared components of the near field E_x^2 and E_z^2 contribute to the signal with appropriate weights [Eq. (20)] (the contribution of E_y^2 is smaller in this

case). Therefore, even if S-polarized detection is selected, in some positions on top of the antenna the z component of the local near field is so strong that it dominates over the x component [see bright spots at the edges, on top of the antenna, in Fig. 4(b) top, for both theory and experiment]. Hence, the maximum of the signal is positioned above the antenna arm and not at the position outside of the antenna, as would be observed for the pristine x component. The quadratic combination of components also explains the zero phase shift observed when crossing the antenna arm. We also observe a jump in the phase in the transverse direction to the antenna axis in the S-polarized detection. This jump is not identified in the theoretical model image, and it might be connected with the tip oscillation close to the antenna's side edge. We demonstrate in the next section that the prediction of our model for the signal captured from the area above the antenna perfectly fits with the experiment.

3.3. Linear versus quadratic combination of components

We analyze in more detail the dependences of the scattered far fields on the local near-field components. Figure 5(a) and (b) depict the calculated line profile of P- and S-polarized scattered far-field amplitudes, respectively, measured along the top center of the single dipolar antennas in Fig. 4. The experimental signal (black line) is compared to the demodulated far-field amplitude and phase profiles obtained theoretically by applying Eq. (22) for a tip of effective radius of 30 nm, tapping amplitude Δ of 85 nm and including the additional influence of the anharmonicity following Eq. (23) with $\delta = 0.05\Delta$.

A remarkable feature of the experimental signal profiles (black lines in Fig. 5) is that the P-polarized amplitude signal exhibits an approximately linear profile with the distance from the antenna center, whereas the signal obtained with S polarization approximately shows a parabolic profile. Equation (21) reveals that the measured P-resolved signal is linearly proportional to the amplitude of the z component of the electric near field above the antenna axis. Other components do not contribute to the signal at the central line of the profile due to symmetry considerations. This is corroborated from the calculation of the amplitude of this component (E_z) along the antenna (blue line in Fig. 5(a), top), showing a linear profile along the antenna from the center. Since the expression for the S-polarized scattered far field in Eq. (20) shows a quadratic dependence on the amplitude of the z component of the electric field, E_z^2, the parabolic experimental profile can be expected for this polarization. This dependence can indeed be verified in the experimental profile of Fig. 5(b) top, black line, with a quadratic profile in agreement with our theoretical predictions (red line). The effects of tapping amplitude demodulation and anharmonicity also influence the fine details of the signal, but the main trends of the linear and quadratic behaviour, as reported here, remain the same (see Supp. Inf. for a comparison of the direct and demodulated signals for different tapping amplitudes and anharmonicity parameters).

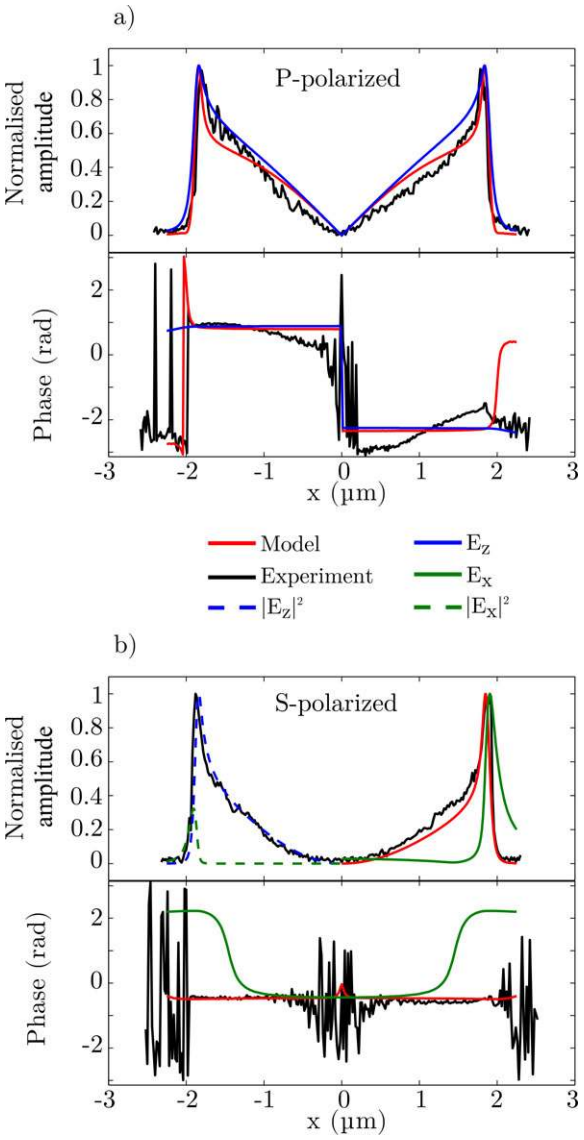

Figure 5 Cross sections of the scattered far-field amplitude and phase along a longitudinal antenna axis for (a) P-polarized and (b) S-polarized detection. The experimental signal (black) is compared with theoretical calculations: near-field components E_x (full line, green color), E_z (full line, blue color) and demodulated signal including anharmonic tip oscillations (red line). The squared amplitudes of the near-field components $|E_x|^2$ (green dashed line) and $|E_z|^2$ (blue dashed line) are included in (b) for comparison. $|E_x|^2$ is normalized to the maximum of $|E_z|^2$. The phase of the near-field components and the model calculations is offset for a better comparison with the experimental data. The antenna length is 3.8 μm.

The phase profiles of both the experimental and the theoretical signals for P-resolved detection [Fig. 5(a), bottom, black and red lines, respectively] exhibit a π shift associated with the dipole mode of the antenna, reproducing the behaviour of the phase of the E_z component (blue line).

A closer observation of the experimental line profile for the phase signal obtained with P polarization (black line) reveals a slight phase gradient towards the center of the antenna, whereas the theoretical signal (red line) predicts a constant phase associated with a sharp phase jump in the center of the antenna. This minor disagreement can be associated with a slight experimental misalignment with respect to the precise geometry considered in the calculations.

For S-polarized detection [Fig. 5(b), bottom], the signal of the experimental phase (black line) can be nicely reproduced by our theoretical model (red line). The constant phase profile on both sides of the antenna verifies the theoretical prediction that the signal obtained with S polarization is mainly given by the weighted sum of the squares of the local near-field components (Fig. 5, dashed lines), and not directly by the in-plane component E_x (green line). The signal on top of the antenna, along its axis, is given in our calculations exclusively by the E_z component of the local near field. The x component of the local near field contributes to the signal only in areas outside of the antenna, but with much smaller weight than for the z component. As a result, the maximum of the signal is located on top of the antenna body, and not on one of the antenna sides.

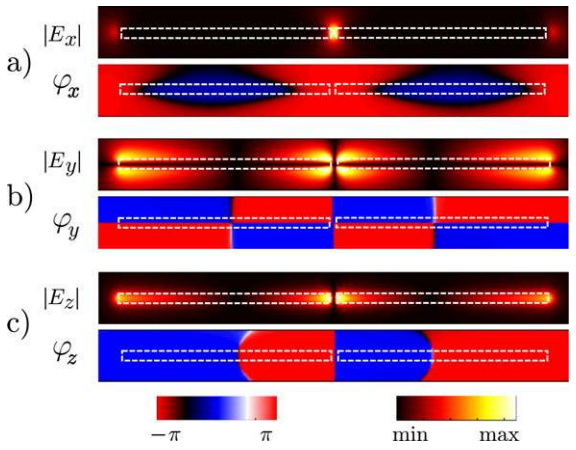

Figure 6 Calculated near-field maps of the amplitude (top) and phase (bottom) of the local near-field components induced on a plane on top of an Au gap antenna. (a) In-plane component, E_x and φ_x, (b) in-plane component, E_y and φ_y, and (c) out-of-plane component, E_z and φ_z. The length of each antenna arm is 3.35 μm with a gap of 30 nm.

4. Near-field maps of gap antennas

We now explore the implications of our model in another important configuration in plasmonics: the system formed by two metallic arms, 3.35 μm long, interacting in close proximity forming a gap nanoantenna (gap $\approx$ 30 nm), as illustrated in the topography image of Fig. 7(a), left. We apply our model to this structure when incident light illuminates the antenna in backscattering mode with incident polarization along the antenna axis (x). A hot spot in between the antenna arms is expected when the antenna is illuminated in resonance, following a strong Coulomb interaction between the two antenna arms [40, 50–54].

We display the calculated local near-field components induced on a plane on top of the gap antenna by light polarized along the antenna axis in Fig. 6. The amplitude (top) and phase (bottom) are displayed for (a) the x component, (b) the y component and (c) the z component. As expected, the x component of the local near field is mainly localized at the antenna gap. Due to the coupling, the y and z components show a slightly asymmetric distribution above each antenna arm, resembling that of single antennas in Fig. 3(b) and (c).

Following the same experimental procedure as in the previous section, polarized s-SNOM images of amplitude and phase are obtained. The results are shown in Figs. 7(b) and (c) for S and P polarization, respectively. For in-plane S-polarized detection, a hot spot can be clearly identified in the antenna gap [top-left image in Fig. 7(b)]. The results of the full theoretical analysis shown in Fig. 7(b), top right, reproduce the intensity of the local near-field amplitude in the antenna gap, as well as on top of the antenna extremities, consistent with the presence of x and z components of the local near field obtained in the S-resolved signal, as derived from Eq. (20). This situation is analogous to the case of the single antennas discussed in Fig. 4(b), top right. Therefore, our results corroborate that the parallel-detection scheme does not straightforwardly map the in-plane x component of the local near field, as one could intuitively assume, but it rather includes a quadratic combination of in-plane and out-of-plane components, E_x and E_z, respectively.

When the detector is polarized along the out-of-plane direction (P), the hot spot at the gap is not visible in the experimental amplitude [Fig. 7(c), top left]; however, regions of large field enhancement on top of the arms of the antenna are distinguishable, decaying towards the center of each arm. Under this detection scheme, and following Eq. (21), the signal is mainly proportional to the out-of-plane (z) component and to the transverse component (y) of the local near field, similar to the case of single linear antennas. A more detailed description of the amplitude profiles along the gap antennas is included in Supp. Inf.

The theoretical images in Fig. 7(c), as well as those in Fig. 4(c) corresponding to single antennas, agree perfectly with the signals observed experimentally, thus emphasizing the importance of a complete description of the scattering process to describe the mapping of plasmonic antennas.

5. Local near field at hot spots: antenna's apex and gap

Optical and infrared antennas produce regions of space where the electromagnetic fields are concentrated and enhanced dramatically, known as *hot spots* [50]. The selection of the component that provides the main contribution to the field enhancement at each point depends on the particular position where the near field is evaluated. In the case of a single linear antenna, the *hot spots* identified are located in the proximity of the antenna extremities (apexes). In the

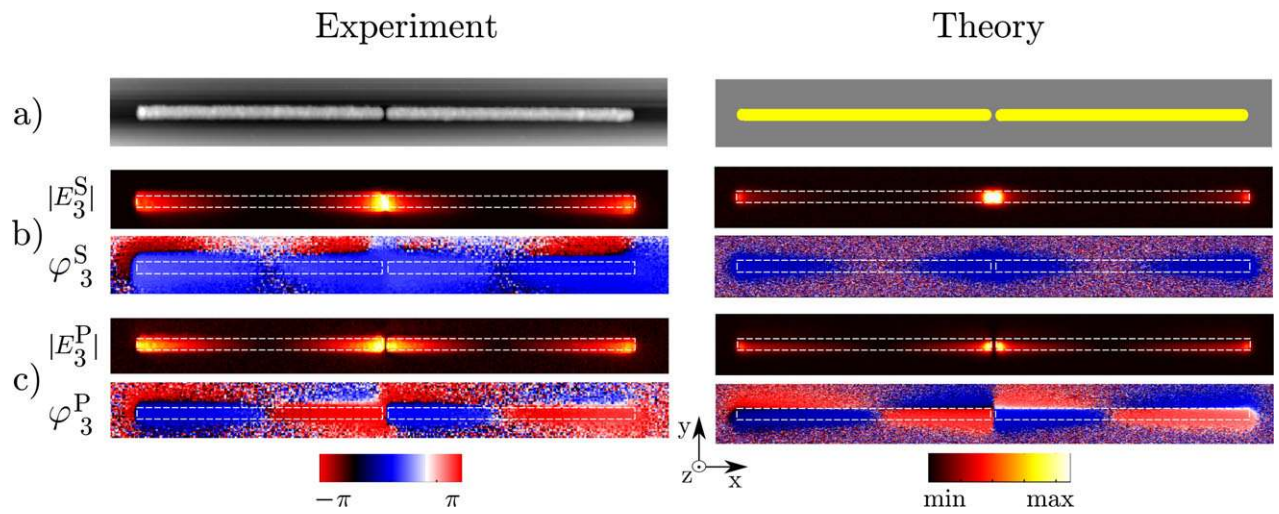

Figure 7 Comparison of experimental and theoretical s-SNOM images in a Au gap antenna. (a) Topography (left) and schematics of the geometry used in the calculations of the local fields around the antenna (right). (b), (c) s-SNOM amplitude $|E_3|$ and phase φ_3 signals obtained with (b) *S*-polarized detection and (c) *P*-polarized detection. Experimental signals are displayed to the left and calculated amplitude $|E_3|$ and phase φ_3 of the demodulated scattered far field from the antenna to the right, in both cases. The demodulated scattered far-field maps are obtained from the evaluation of the expressions in Eqs. (18) and (19) together with Eq. (22). Anharmonicity and noise have also been included as described in the text. The length of each antenna arm is 3.35 μm with a gap of $\approx$ 30 nm. The theoretical images are calculated assuming an effective tip radius of 30 nm, a tapping amplitude of $\Delta = 85$ nm and an anharmonicity parameter of $\delta = 0.05\Delta$. The signal amplitude is saturated in (b).

apex area, on top of the metal, the component of the local near field governing the enhancement is the out-of-plane component (z component); therefore, we can approximate the signal that combines the local near-field components in Eqs. (20) and (21) by simplified expressions that consider only the large component. In a region in the proximity of the antenna where the out-of-plane component (z) is very large, $E_z >> E_x$, and $E_z >> E_y$, and therefore at these special positions of the linear antennas (*hot spots*), the expressions for the *P*- and *S*-resolved signals can be simplified to

$$E_n^S \propto \alpha_z^T \left(E_z^2\right)_n / E^I = \alpha_z^T \left(f_z^2\right)_n \cdot E^I \qquad (24)$$

and

$$E_n^P \propto \alpha_z^T (E_z)_n = \alpha_z^T (f_z)_n \cdot E^I. \qquad (25)$$

According to Eqs. (24) and (25), at the extremities of a linear antenna on top of the metal, *P* polarization measures a linear dependence of the signal on the out-of-plane near-field component, whereas *S*-polarized detection measures a quadratic dependence on the out-of-plane component. The result in Eq. (24) implies that it is possible to map the out-of-plane component of the local field in an antenna with *S*-polarized detection. This situation can be experimentally observed in both single antennas [Fig. 4(b), top left] and gap antennas [Fig. 7(b), top left], where substantial signal from the z component is mapped in *S*-polarization detection. It can thus happen that the selection of a particular position to evaluate the local near field can provide information of an unexpected component, as in this case: at the antenna hot spot (antenna extremity), the in-plane-polarized detection scheme provides information on the out-of-plane local near-field component.

In a gap antenna, an additional *hot spot* appears at the gap, where the in-plane x component of the local near field E_x is very large. At the antenna gap, the expression for the *P*-resolved signal in Eq. (21) implies that the signal involves only information on the y and z components of the local near fields. However, for *S*-polarized detection, the small components in Eq. (20) can be neglected; thus, the signal from the gap yields information on the in-plane component E_x, following the expression

$$E_n^S \propto \alpha_x^T (E_x^2)_n / E^I = \alpha_x^T \left(f_x^2\right)_n \cdot E^I. \qquad (26)$$

Hence, for a strong in-plane local near-field enhancement, *S*-polarized detection resolves a quadratic dependence of the in-plane local near field.

This interpretation is corroborated by the calculated signal obtained from Eq. (22) and the experimental map obtained for the case of *S*-polarized detection, shown in Fig. 7(b), top right and top left, respectively, where both the antenna gap and the extremities appear with considerable intensity. The signals obtained at both positions of the gap antenna might be equally intense, but the origin of this intensity is totally different: at the gap, the intensity is proportional to the square of the in-plane near-field enhancement [Eq. (26)], whereas on top of the arms' extremities, the signal is proportional to the square of the out-of-plane near-field component [Eq. (20)], as described previously.

The correct assignment of the local near-field components to the corresponding polarization-resolved signal thus

depends on the actual position of evaluation at the antenna, as well as on the particular relative intensity of each of the local near-field components, as demonstrated here both by theory and experiments.

6. Conclusion

Based on electromagnetic scattering theory applied to the system of a sample antenna and a probing tip, we have developed a new formalism to correctly interpret polarization-resolved s-SNOM images, which is fully corroborated by experiments. Contrary to what had been considered in previous studies, we have shown that the demodulated signal cannot be simply related to a specific near-field component. The signal measured in s-SNOM at a given position involves a weighted sum of the individual local near-field components at that position. The weighting factors are spatially dependent and can be obtained from a combination of the polarizability tensor components of the probing tip with the components of a virtual local near-field distribution. The virtual near fields are produced by an imaginary source positioned at the detector, with the polarization determined by the orientation of the analyzer.

We have applied our generalized model to the examples of linear and gap-plasmonic nanoantennas for a specific but typical detection and illumination scheme. Our model shows an excellent agreement with the experimental images, explaining features in the plasmonic maps that remained poorly understood to date. For the analyzed systems and incidence polarization scheme, the new model predicts that the S-resolved signal provides information of a linear combination of squared local near-field components of the antenna, whereas the P-resolved signal produces experimental maps given by a linear combination of the near-field components. This interpretation of the P- and S-resolved signals is derived for linear plasmonic antennas for the particular conditions of in-plane illumination and backscattering detection; however, measurements with other illumination/detection schemes can be equally interpreted with use of the general formalism presented here. The complex-valued combination of near-field components involved in a general s-SNOM signal can lead to surprisingly distributed near-field maps, which are impossible to interpret solely in terms of the isolated near-field components induced at the antennas.

The results presented here set a robust basis for a general interpretation of s-SNOM near-field maps. Furthermore, our formalism might also provide new insights to interpret the signals obtained in antenna-assisted molecular fluorescence [55], near-field tomography techniques [32] or in the development and better understanding of field-enhanced spectroscopies [45–47] mediated by plasmonic antennas, where the concepts presented here might also apply.

Supporting Information

Additional supporting information may be found in the online version of this article at the publisher's website.

Acknowledgement. Projects FIS2013-41184P and MAT2012-36580 of the Spanish Ministry of Economy and Competitiveness, as well as project *CORROPTO* ETORTEK-2014 of the Department of Industry of the Basque Government, are acknowledged.

Received: 4 February 2015, **Revised:** 17 June 2015,
Accepted: 29 September 2015

Published online: 4 November 2015

Key words: plasmonics, optical nanoantennas, scattering theory, scattering-type near-field optical microscopy, s-SNOM.

References

[1] P. Muhlschlegel, H. J. Eisler, O. J. F. Martin, B. Hecht, and D. W. Pohl, Science **308**(5728), 1607–1609 (2005).
[2] M. Pelton, J. Aizpurua, and G. Bryant, Laser & Photonics Rev. **2**(3), 136–159 (2008).
[3] P. Bharadwaj, B. Deutsch, and L. Novotny, Adv. Opt. Photon. **1**(3), 438–483 (2009).
[4] H. Xu, E. J. Bjerneld, M. Käll, and L. Börjesson, Phys. Rev. Lett. **83**(21), 4357–4360 (1999).
[5] R. Zhang, Y. Zhang, Z. C. Dong, S. Jiang, C. Zhang, L. G. Chen, L. Zhang, Y. Liao, J. Aizpurua, Y. Luo, J. L. Yang, and J. G. Hou, Nature **498**, 82–86 (2013).
[6] M. Abb, P. Albella, J. Aizpurua, and O. L. Muskens, Nano Letters **11**(6), 2457–2463 (2011).
[7] O. Hess, J. B. Pendry, S. A. Maier, R. F. Oulton, J. M. Hamm, and K. L. Tsakmakidis, Nature Mater. **11**(7), 573–584 (2012).
[8] J. N. Anker, W. P. Hall, O. Lyandres, N. C. Shah, J. Zhao, and R. P. Van Duyne, Nature Mater. **7**(6), 442–453 (2008).
[9] R. Adato and H. Altug, Nat. Commun. (4), 2154 (2013).
[10] S. Lal, S. E. Clare, and N. J. Halas, Accounts of Chemical Research **41**(12), 1842–1851 (2008).
[11] H. A. Atwater and A. Polman, Nature Mater. **9**(3), 205–213 (2010).
[12] C. Berry, N. Wang, M. Hashemi, M. Unlu, and M. Jarrahi, Nature Mater. **4**, 1622 (2013).
[13] A. Merlen and F. Lagugné-Labarthet, App. Spec. OA **62**(12), 1307–1326 (2014).
[14] J. Nelayah, M. Kociak, O. Stephan, F. J. Garcia de Abajo, M. Tence, L. Henrard, D. Taverna, I. Pastoriza-Santos, L. M. Liz-Marzan, and C. Colliex, Nature Phys. **3**(5), 348–353 (2007).
[15] U. Hohenester, H. Ditlbacher, and J. R. Krenn, Phys Rev. Lett. **103**(10), 106801 (2009).
[16] M. Burresi, D. van Oosten, T. Kampfrath, H. Schoenmaker, R. Heideman, A. Leinse, and L. Kuipers, Science **326**(5952), 550–553 (2009).
[17] H. Gersen, L. Novotny, L. Kuipers, and N. F. van Hulst, Nature Photon. **1**(5), 242 (2007).
[18] R. Hillenbrand, F. Keilmann, P. Hanarp, D. S. Sutherland, and J. Aizpurua, Appl. Phys. Lett. **83**(2), 368–370 (2003).
[19] K. G. Lee, H. W. Kihm, J. E. Kihm, W. J. Choi, H. Kim, C. Ropers, D. J. Park, Y. C. Yoon, S. B. Choi, D. H. Woo, J. Kim, B. Lee, Q. H. Park, C. Lienau, and D. S. Kim, Nature Photon. **1**(1), 53–56 (2007).

[20] R. Esteban, R. Vogelgesang, J. DorfmuÌller, A. Dmitriev, C. Rockstuhl, C. Etrich, and K. Kern, Nano Lett. **8**(10), 3155–3159 (2008).
[21] M. Rang, A. C. Jones, F. Zhou, Z. Y. Li, B. J. Wiley, Y. Xia, and M. B. Raschke, Nano Lett. **8**(10), 3357–3363 (2008).
[22] Z. H. Kim and S. R. Leone, Opt. Express **16**(3), 1733–1741 (2008).
[23] M. Schnell, A. Garcia-Etxarri, J. Alkorta, J. Aizpurua, and R. Hillenbrand, Nano Lett. **10**(9), 3524–3528 (2010).
[24] R. L. Olmon, M. Rang, P. M. Krenz, B. A. Lail, L. V. Saraf, G. D. Boreman, and M. B. Raschke, Phys. Rev. Lett. **105**, 167403 (2010).
[25] P. Alonso-Gonzalez, M. Schnell, P. Sarriugarte, H. Sobhani, C. Wu, N. Arju, A. Khanikaev, F. Golmar, P. Albella, L. Arzubiaga, F. Casanova, L. E. Hueso, P. Nordlander, G. Shvets, and R. Hillenbrand, Nano Lett. **11**(9), 3922–3926 (2011).
[26] S. Mastel, S. E. Grefe, G. B. Cross, A. Taber, S. Dhuey, S. Cabrini, P. J. Schuck, and Y. Abate; Appl. Phys. Lett. **101**(13), 131102 (2012).
[27] P. Alonso-González, P. Albella, M. Schnell, J. Chen, F. Huth, A. García-Etxarri, F. Casanova, F. Golmar, L. Arzubiaga, L. E. Hueso, J. Aizpurua, and R. Hillenbrand, Nat. Commun. **3**, 684 (2012).
[28] S. E. Grefe, D. Leiva, S. Mastel, S. D. Dhuey, S. Cabrini, P. J. Schuck, and Y. Abate, Phys. Chem. Chem. Phys. **15**(43), 18944–18950 (2013).
[29] T. G. Habteyes, J. Phys. Chem. C **118**(17), 9119–9127 (2014).
[30] R. Hillenbrand and F. Keilmann, Phys. Rev. Lett. **85**(14), 3029–3032 (2000).
[31] J. A. Porto, P. Johansson, S. P. Apell, and T. López-Ríos, Phys. Rev. B **67**(8), 085409 (2003).
[32] J. Sun, P. S. Carney, and J. C. Schotland, J. Appl. Phys. **102**(10), 103103 (2007).
[33] A. J. Huber, F. Keilmann, J. Wittborn, J. Aizpurua, and R. Hillenbrand, Nano Lett. **8**(11), 3766–3770 (2008).
[34] J. M. Stiegler, A. J. Huber, S. L. Diedenhofen, J. Gómez Rivas, R. E. Algra, E. P. A. M. Bakkers, and R. Hillenbrand, Nano Lett. **10**(4), 1387–1392 (2010).
[35] A. García-Etxarri, I. Romero, F. J. García de Abajo, R. Hillenbrand, and J. Aizpurua, Phys. Rev. B **79**(12), 125439 (2009).
[36] J. Dorfmüller, D. Dregely, M. Esslinger, W. Khunsin, R. Vogelgesang, K. Kern, and H. Giessen, Nano Lett. **11**(7), 2819–2824 (2011).
[37] J. J. Greffet and R. Carminati, Prog. Surf. Sci. **56**(3), 133–237 (1997).
[38] R. Esteban, R. Vogelgesang, and K. Kern, Phys. Rev. B **75**(19), 195410 (2007).
[39] J. Dorfmüller, R. Vogelgesang, R. T. Weitz, C. Rockstuhl, C. Etrich, T. Pertsch, F. Lederer, and K. Kern, Nano Lett. **9**(6), 2372–2377 (2009).
[40] M. Schnell, A. García-Etxarri, A. J. Huber, K. Crozier, J. Aizpurua, and R. Hillenbrand, Nature Photon. **3**(5), 287–291 (2009).
[41] D. S. Kim, J. Heo, S. H. Ahn, S. W. Han, W. S. Yun, and Z. H. Kim, Nano Lett. **9**(10), 3619–3625 (2009).
[42] J. Dorfmüller, R. Vogelgesang, W. Khunsin, C. Rockstuhl, C. Etrich, and K. Kern, Nano Lett. **10**(9), 3596–3603 (2010).
[43] J. A. Porto, R. Carminati, and J. J. Greffet, J. Appl. Phys. **88**(8) 4845–4850 (2000).
[44] M. Esslinger and R. Vogelgesang, ACS Nano **6**(9), 8173–8182 (2012).
[45] F. Neubrech and A. Pucci, IEEE J. Sel. Topics Quantum Electron. **19**(3), 4600809 (2013).
[46] F. Neubrech, A. Pucci, T. W. Cornelius, S. Karim, A. García-Etxarri, and J. Aizpurua, Phys. Rev. Lett. **101**(15), 157403 (2008).
[47] L. V. Brown, K. Zhao, N. King, H. Sobhani, P. Nordlander, and N. J. Halas, J. Am. Chem. Soc. **135**(9), 3688–3695 (2013).
[48] R. Hillenbrand, M. Stark and R. Guckenberger, Appl. Phys. Lett. **76**(23), 3478–3480 (2000).
[49] Lumerical Solutions, Inc. https://www.lumerical.com/tcad-products/fdtd/, (October 2015).
[50] H. Xu, J. Aizpurua, M. Käll, and P. Apell, Phys. Rev. E **62**(3), 4318–4324 (2000).
[51] P. Nordlander, C. Oubre, E. Prodan, K. Li, and M. I. Stockman, Nano Lett. **4**(5), 899–903 (2004).
[52] I. Romero, J. Aizpurua, G. W. Bryant, and F. J. García de Abajo, Opt. Express **14**(21), 9988–9999 (2006).
[53] E. Cubukcu, E. A. Kort, K. B. Crozier, and F. Capasso, Appl. Phys. Lett. **89**(9), 093120 (2006).
[54] O. Pérez-González, N. Zabala, A. G. Borisov, N. J. Halas, P. Nordlander, and J. Aizpurua, Nano Lett. **10**(8), 3090–3095 (2010).
[55] A. Singh, G. Calbris, and N. F. van Hulst, Nano Letters **14**(8), 4715–4723 (2014).